NANO LETTERS

pubs.acs.org/NanoLett

Letter

Nanoimaging of Low-Loss Plasmonic Waveguide Modes in a Graphene Nanoribbon

Wenyu Zhao,[¶] Hongyuan Li,[¶] Xiao Xiao, Yue Jiang, Kenji Watanabe, Takashi Taniguchi, Alex Zettl, and Feng Wang*

Cite This: *Nano Lett.* 2021, 21, 3106−3111

Read Online

ACCESS | Metrics & More | Article Recommendations | Supporting Information

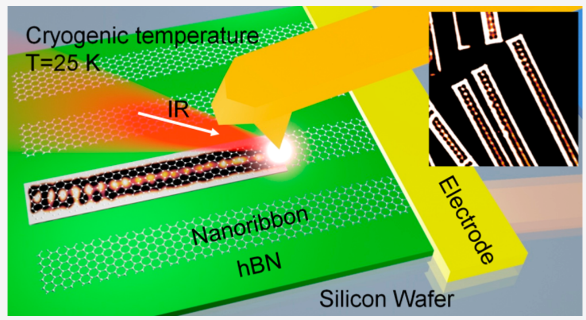

ABSTRACT: Graphene nanoribbons are predicted to support low-loss and tunable plasmonic waveguide modes with an ultrasmall mode area. Experimental observation of the plasmonic waveguide modes in graphene nanoribbons, however, is challenging because conventional wet lithography has difficulty creating a clean graphene nanoribbon with a low edge roughness. Here, we use a dry lithography method to fabricate ultraclean and low-roughness graphene nanoribbons, which are then encapsulated in hexagonal boron nitride (hBN). We demonstrate low-loss plasmon propagation with a quality factor up to 35 in the ultraclean nanoribbon waveguide using cryogenic infrared nanoscopy. In addition, we observe both the fundamental and the higher-order plasmonic waveguide modes for the first time. All the plasmon waveguide modes can be tuned through electrostatic gating. The observed tunable plasmon waveguide modes in ultraclean graphene nanoribbons agree well with the finite-difference time-domain (FDTD) simulation results. They are promising for reconfigurable photonic circuits and devices at a subwavelength scale.

KEYWORDS: *Graphene nanoribbon, Plasmonic waveguide modes, Near-field nanoscopy, Photonic circuit*

INTRODUCTION

The surface plasmon polariton (SPP), coupled with electromagnetic and surface charge oscillations, has the unique capability to confine and manipulate light at the subwavelength scale.[1] The strong field enhancement and decreased mode volume dramatically increase the light−matter interaction and play a key role in nano-optics[2−4] ranging from nanoscale transform optics[5] and quantum optics[6] to flat optics.[7] A key building block of plasmonic nanodevices is the plasmonic waveguide, which connects different units in the photonic circuits. Many plasmonic waveguides based on noble metals have been proposed such as slot waveguides,[8] planar waveguides,[9] and hybrid waveguides.[10] However, metal intrinsically suffers from strong Ohmic loss and poor field confinement, which creates the bottleneck to achieving high performance devices. Compared with its metallic counterpart, the graphene plasmonic waveguide is a promising candidate due to the low propagation loss and small footprint.[11−20] The waveguide mode in the graphene nanoribbon features ultrahigh field confinement orders larger than that in metal ($\lambda_p/\lambda_0 \sim 1/150$).[21−25] In addition, the graphene nanoribbon can be easily tuned and controlled either by applying an electrostatic bias or by chemical doping.[15] Theoretical studies have revealed that a set of low-loss plasmonic modes can propagate in graphene nanoribbon waveguides.[5,12,14,26] However, the experimental study of the low-loss plasmon propagation in the graphene nanoribbon is challenging because standard lithography methods tend to introduce unintended polymer residues and defects on the graphene surface.[13,16] The one-atom-thickness graphene nanoribbon is extremely sensitive to those imperfections, which strongly degrades the plasmon quality. In previous studies, the plasmon quality factor in lithographically fabricated graphene nanoribbons is often lower than 4.[11,13,16,27]

In this letter, we report the direct observation of the ultralong propagation of plasmonic waveguide modes in an encapsulated ultraclean graphene nanoribbon at cryogenic temperature. We use an atomic force microscope (AFM) based dry lithography method to fabricate the ultraclean graphene nanoribbon and then encapsulate it with two hBN flakes to further increase the device quality. The plasmon modes in the nanoribbon are imaged by a cryogenic nanoscopy setup at 25 K to suppress the dissipation from the phonon scattering. At

Received: January 22, 2021
Revised: March 1, 2021
Published: March 17, 2021

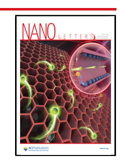

https://doi.org/10.1021/acs.nanolett.1c00276
Nano Lett. 2021, 21, 3106−3111

high electron doping the nanoribbon exhibits low-loss plasmon waveguide modes with a quality factor up to 35. Both the fundamental and high-order waveguide modes can be clearly resolved in real space and can be tuned by electrostatic gating. Our experimental observations agree well with the FDTD simulation results of the graphene nanoribbons.

■ RESULTS AND DISCUSSION

We fabricate clean graphene nanoribbons using the AFM-based dry lithography developed in ref 28. In this AFM-based lithography, a high-frequency (>10 kHz) alternating voltage applied to the conductive AFM tip drives a local anodic oxidation process that etches the graphene right below the tip. It does not introduce any contaminants such as photoresists or developers present in conventional lithography. The AFM-based lithography can readily etch an arbitrary pattern in graphene with superior edge smoothness, resulting in ultraclean graphene nanoribbons with an RMS edge roughness of 1.5 nm[29] (see Supporting Information). After fabricating the graphene into the periodic nanoribbon arrays shown in Figure 1a, the ultraclean graphene nanoribbon is then encapsulated by two hBN flakes using the dry-transfer technique (see Methods for details). We use an ultrathin top hBN with a thickness of ∼2 nm so that the near-field probe can access the graphene plasmon in infrared nanoscopy. The heterostructure is finally released onto a SiO_2 (285 nm)/Si substrate. The gate electrode (5 nm Cr/100 nm gold) is deposited by e-beam evaporation through a shadow mask to avoid contamination on the device surface from nanofabrication. Figure 1b shows the optical image of the final graphene nanoribbon array device, where the graphene nanoribbon area is denoted by the red dashed box.

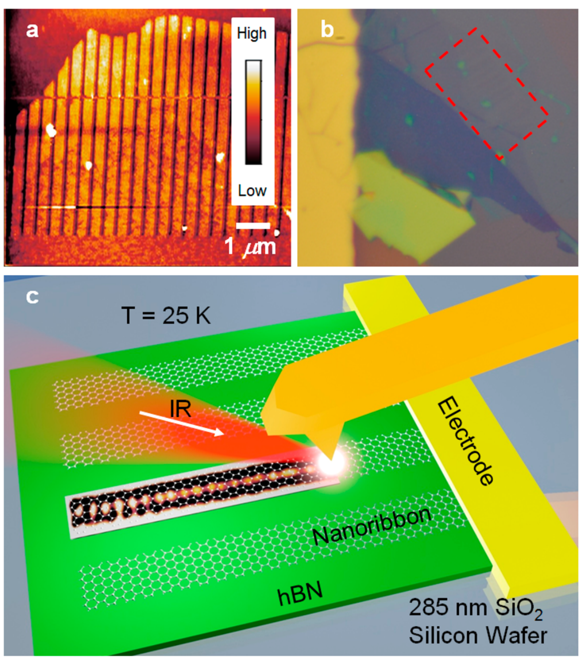

Figure 1. Infrared nanoimaging of plasmonic waveguide modes in the graphene nanoribbon. (a) AFM topography image of an array of graphene nanoribbons fabricated by the AFM lithography. The nanoribbon array has a periodicity of 400 nm and width of 300 nm. (b) Optical image of the graphene nanoribbon device. The optical contrast of the graphene nanoribbon becomes weak after the hBN encapsulation. The nanoribbon area is indicated by the red dashed line. (c) Schematic view of the cryogenic nanoscopy technique. The CO_2 laser is focused onto the sharp tip of an AFM system in a vacuum. The sample together with the AFM is cooled down to low temperature by a closed cycle cryostat. In this letter, all the measurements are collected with a fixed temperature at 25 K.

We probe the low-loss plasmon waveguide modes in ultraclean graphene nanoribbons using cryogenic near-field infrared nanoscopy. Figure 1c shows the schematic view of our near-field infrared nanoscopy technique to image the plasmonic modes in the nanoribbon.[21,22,24,30] A 10.6 μm CO_2 laser was focused on the tip by an aspheric ZnSe lens with a spot size around 10 μm. The gold coated tip can compensate the momentum mismatch between the plasmon and the free space light and efficiently excite different plasmon modes in the graphene nanoribbon. The plasmons excited by the tip propagate along the nanoribbon and get reflected at the nanoribbon end. The forward and backward propagating plasmons generate an interference pattern of standing waves imprinted with the characteristic plasmon wavelengths and quality factors of different modes. The tip also acts as an antenna to pick up the local optical intensity and scatters it into the far field, which is then detected by a HgCdTe (MCT) detector. By scanning along the graphene nanoribbon and recording the near-field interference fringes, we can study the different plasmon modes supported by the nanoribbon in real space.

At ambient conditions, plasmonic dissipation in graphene is substantial and limits the propagation of plasmonic waveguide modes in the nanoribbon.[22] In order to improve the quality factor of the graphene plasmons, we cooled the sample and the AFM down to cryogenic temperature using a closed-cycle cryostat. The temperature of the sample is fixed at 25 K during the measurements, and the phonon scattering of the graphene plasmon is strongly suppressed, resulting in a high plasmon quality factor.[22]

Figure 2a shows the topography of the hBN encapsulated nanoribbon device at 25 K. The root-mean-square (RMS) noise in the topography channel is around 0.24 nm, which guarantees a stable scanning even at low temperature. Figure 2b−h shows the near-field images of 300 nm wide graphene nanoribbons under different gate voltages at 25 K. We notice that some nanoribbons get strongly distorted during the mechanical transfer and stacking processes. Our study will focus on a straight isolated nanoribbon that can be efficiently gated. At low carrier doping with Vg = 30 V, no well-defined plasmon waveguide mode in the nanoribbon can be observed (Figure 2b). The edges of the nanoribbon do show a strong enhancement of the near-field signal. Presumably this comes from the excitation of the edge plasmon modes, similar to that observed at the edge of two-dimensional graphene sheets. The plasmon waveguide modes start to appear at Vg > 45 V, and they become more prominent with higher doping at increased gate voltages. At Vg = 60 and 75 V, the most prominent mode in the near-field nanoscopy image is a second-order plasmon waveguide mode, where there are two maxima along the nanoribbon width direction (Figure 2d,e). At Vg higher than 90 V, the fundamental plasmon waveguide mode dominates the near-field response, which exhibits a very long propagation length (Figure 2g,h). To better examine the low-loss plasmon propagation, we plot in Figure 2i the one-dimensional near-

https://doi.org/10.1021/acs.nanolett.1c00276
Nano Lett. 2021, 21, 3106−3111

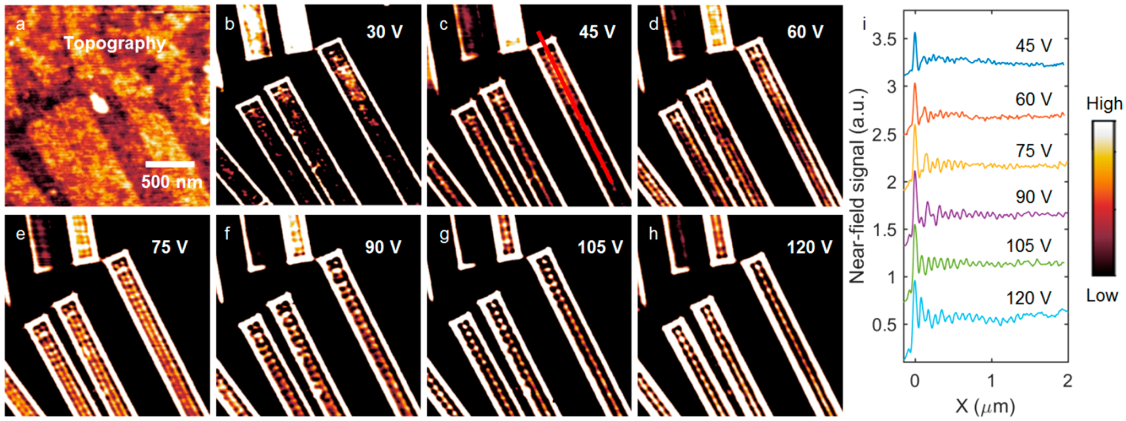

Figure 2. Gate-tunable plasmonic waveguide modes in the graphene nanoribbon. (a) AFM topography of the graphene nanoribbon device recorded simultaneously with the near-field data at low temperature (30 V gating voltage). After the hBN encapsulation, the nanoribbon edge becomes hard to distinguish in the topography. (b−h) Near-field images at different gating voltages from 30 to 120 V. Plasmons in the nanoribbon can be continuously tuned by means of electrostatic gating. With increasing gate voltage and thus a higher Fermi level, the plasmon wavelength increases and the quality factor and propagation length also shows concomitant growth. (i) Line profile of the near-field signal along the nanoribbon indicated by the red line in (c) at various gating voltages.

field signal along the red line in Figure 2c after averaging over the width of the nanoribbon. In order to extract the quality factor, Q, of the plasmon mode, the near-field profile can be fitted with an exponential decay of the form $e^{-2\pi x/(Q\cdot\lambda_p)}\sin((4\pi x)/\lambda_p)$. At Vg = 120 V, the plasmon shows an ultralong propagation length with quality factor Q = 35. To our best knowledge, this is the highest quality factor observed for plasmon waveguide modes in graphene nanoribbons. We noticed that, due to the edge roughness of the nanoribbon, the plasmon Q factor in this patterned graphene nanoribbon is still lower than that of the plasmon supported by sheet graphene.[22] As the graphene channel becomes narrow, the edge roughness introduces another damping channel to the plasmon dissipation.

To understand the gate-dependent plasmon waveguide modes, we calculate the plasmonic eigenstates in graphene nanoribbons using FDTD simulations. Figure 3a shows the field distribution of different plasmonic modes along the nanoribbon width direction calculated by FDTD using the Lumerical software package. In the simulations, the graphene is treated as a 2D surface with a conductivity extracted from the Kubo formula (see Methods for the simulation details). The graphene nanoribbon can support several plasmonic waveguide modes with low propagation loss, as shown in Figure 3a. The different modes are labeled according to the number of nodes inside the nanoribbon. For the fundamental waveguide mode, A mode, the field only has one maximum and no node along the width direction of the nanoribbon. One or more nodes are present for higher order plasmonic waveguide modes.

In order to simulate the wave propagation along the nanoribbon, we use a light source placed 3 μm away from the nanoribbon end to excite specific plasmon waveguide modes. The plasmon propagates to the nanoribbon end and gets reflected, which then interferes with the forward plasmon and forms a standing wave. Since the SNOM tip is more sensitive to the out-plane field component, we plot the out-plane field intensity, $|E_Z|^2$, above the nanoribbon for different plasmonic waveguide modes in Figure 3b. In the simulations, one can excite a specific mode by injecting the light with the corresponding field distribution. But in experiment, the momentum provided by the sharp tip can excite several plasmonic modes in the nanoribbon at the same time. Figure 3c shows the near-field infrared nanoscopy image of a representative graphene nanoribbon at Vg = 60 V, which arises from a superimposition of all the possible modes supported by the nanoribbon. We can extract the different plasmonic waveguide modes using two-dimensional (2D) Fourier transformation. Figure 3d shows the 2D Fourier transform of the near-field data in Figure 3c. Along the nanoribbon direction the Fourier transform data shows multiple peaks, and each corresponds to the periodic modulation of a different plasmon waveguide mode (Figure 3e). The near-field contribution of each mode can be extracted by the inverse Fourier transform of the selected area in the spatial frequency domain. Figure 3f shows the near-field contribution of A−D modes obtained by the inverse Fourier transform of the corresponding area denoted by the rectangular boxes in Figure 3d. Different modes show their characteristic near-field patterns and agree well with the simulation results at the same Fermi level. The longitudinal wavelengths for the A−D modes are 134, 152, 193, and 272 nm, respectively, at Vg = 60 V.

Figure 4a shows the evolution of the plasmon wavelength of different modes as a function of the graphene chemical potentials. The solid lines are predictions from FDTD simulation, and the symbols show the extracted wavelengths from the experimental data. The experiment data agree well with the simulation results. The higher-order modes exhibit a cutoff behavior at high doping. This is because the wavelength increases as the doping level increases, and to a certain level the nanoribbon can no longer support a higher-order mode. We noticed that, for some ribbons, a certain mode will dominate the plasmon response at a specific doping level, presumably due to the local variations in excitation efficiency for different modes. Figure 4b shows the near-field data of one nanoribbon at four different gating voltages. As we change the gating voltages, different waveguide modes start to dominate the response with an enhanced characteristic near-field pattern in this nanoribbon: the D mode dominates at Vg = 30 V, the C mode can be clearly observed at Vg = 45 V, the B mode is

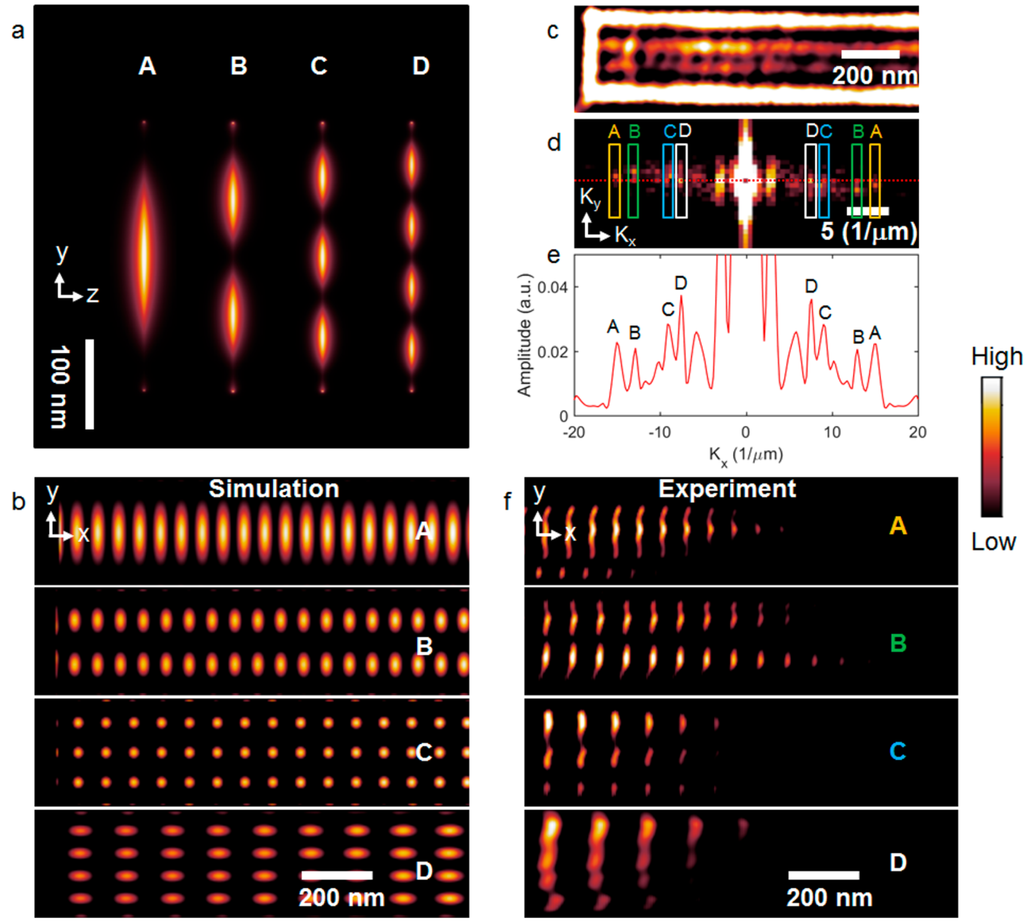

Figure 3. Plasmonic waveguide mode analysis in the graphene nanoribbon. (a) Mode field distribution of different plasmonic modes along the ribbon width direction. The graphene nanoribbon supports a series of plasmonic waveguide modes (A–D). (b) Numerical simulations of different plasmonic waveguide modes propagation in the graphene nanoribbon. The plasmonic modes excited by mode source propagate along the nanoribbon and form a signature interference pattern with the reflected plasmon from the nanoribbon edge. In the calculations, the chemical potential is set at 0.26 eV, corresponding to a gate voltage of 60 V. (c) Near-field infrared nanoscopy image of a representative graphene nanoribbon at Vg = 60 V. (d) 2D Fourier transform of the raw data in (c). (e) Line cut of the Fourier transform data indicated by the red dashed line in (d). The Fourier transform data show multiple peaks corresponding to different nanoribbon waveguide modes. (f) Extraction of the near-field distribution of different modes by the inverse Fourier transform of the selected modes indicated in (d). The wavelengths for the A–D modes (Vg = 60 V) are 134, 152, 193, and 272 nm, respectively.

most prominent at 60 V, and the fundamental mode (A mode) dominates at the highest doping level with Vg = 120 V.

CONCLUSION

In conclusion, we have experimentally studied the ultralong propagation of plasmonic waveguide modes in the graphene nanoribbon. The AFM lithography of graphene allows us to prepare ultraclean graphene nanoribbon samples. Combining this with the cryogenic nanoscopy technique, we observed an unprecedented graphene plasmonic mode with a Q factor up to 35, setting a record for highly confined and tunable polariton modes. By varying the gating voltages, we can also probe the mode evolution from the high-order mode to the fundamental mode. The proposed AFM lithography can be extended to fabricate an arbitrary graphene pattern and directly make graphene based devices in situ. The graphene nanoribbon with an ultrasmall mode area and long propagation length provides a promising platform to construct future photonic circuits and devices.

METHODS

Devices Preparation. Monolayer graphene samples were mechanically exfoliated from graphite onto a SiO_2 (285 nm)/Si substrate. The graphene is then fabricated into a nanoribbon by AFM lithography. We used a dry transfer method with a propylene carbonate (PPC) stamp to fabricate the hBN encapsulated nanoribbon sample. Thin hBN (2 nm), graphene nanoribbon, and thick layer hBN were picked up in sequence. Electrical contacts of Cr/Au (5/100 nm) are fabricated by stencil mask evaporation on the exposed graphene area.

Infrared Nanoimaging of Plasmonic Waveguide Modes. The infrared nanoimaging technique is based on a homemade AFM which has the capability to work at high vacuum and low temperature. The whole AFM setup was built inside a closed cycle cryostat, and the AFM head is connected

https://doi.org/10.1021/acs.nanolett.1c00276
Nano Lett. 2021, 21, 3106–3111

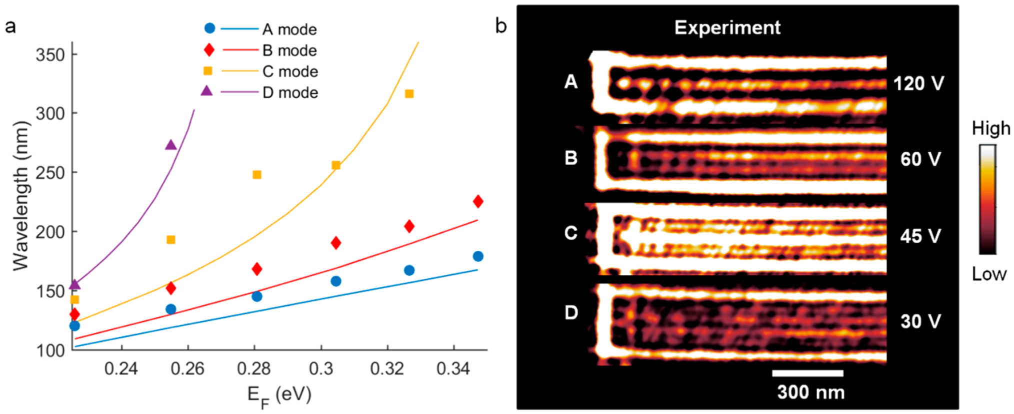

Figure 4. Plasmonic waveguide modes at various gating voltages. (a) Plasmon wavelengths of different waveguide modes in the graphene nanoribbon extracted from simulation and experiment. The high-order waveguide mode shows a strong cutoff behavior with the increased Fermi energy. (b) Near-field data of different plasmonic waveguide modes in one graphene nanoribbon. The fundamental and high-order plasmon waveguide modes can dominate the near-field infrared nanoscopy image at different gate voltages in this nanoribbon.

to the cold plate by a soft copper braid in order to damp the vibration from the pulse tube. The lowest sample temperature achieved in our AFM system is 25 K. We focus an infrared light beam (λ = 10.6 μm) onto the apex of a conductive AFM tip. The enhanced optical field at the tip apex interacts with graphene underneath the tip and is scattered by the tip, carrying the local optical information on the sample. The back scattered light from the tip was collected by MCT in a self-homodyne configuration, and the near-field signal was demodulated at the third harmonic of the tapping frequency to suppress the background. Near-field images are recorded simultaneously with the topography information during the measurements. During the scanning, the turbo pump was turned off in order to minimize the mechanical vibration. The background vacuum level remains below 1×10^{-6} mbar through all the measurements.

Numerical Simulations of Plasmonic Waveguide Modes. The numerical simulations are conducted based on the finite-difference time-domain (FDTD) method with a commercial software package from Lumerical Inc. Graphene is treated as a 2D surface with the conductivity of

$$\sigma(\omega, \Gamma, \mu_c, T) = \sigma_{\mathrm{intra}}(\omega, \Gamma, \mu_c, T) + \sigma_{\mathrm{inter}}(\omega, \Gamma, \mu_c, T))$$

$$\sigma_{\mathrm{intra}}(\omega, \Gamma, \mu_c, T) = \frac{-ie^2}{\pi\hbar^2(\omega + i2\Gamma)} \int_0^\infty \xi\left(\frac{\partial f_d(\xi)}{\partial \xi} - \frac{\partial f_d(-\xi)}{\partial \xi}\right) d\xi$$

$$\sigma_{\mathrm{inter}}(\omega, \Gamma, \mu_c, T) = ie^2(\omega + i2\Gamma)\pi\hbar^2 \int_0^\infty f_d(-\xi) - f_d(\xi)(\omega + i2\Gamma)^2 - 4\left(\frac{\xi}{\hbar}\right)^2 d\xi$$

$$f_d(\xi) \equiv 1/\exp((\xi - \mu_c)/(k_B T)) + 1$$

ω, Γ, μ_c, and T are the angular frequency, scattering rate, chemical potential, and temperature, respectively. e, $\hbar$ and k_B are the electron charge, reduced Plank constant, and Boltzmann constant.

ASSOCIATED CONTENT

Supporting Information

The Supporting Information is available free of charge at https://pubs.acs.org/doi/10.1021/acs.nanolett.1c00276.

Graphene nanoribbon edge roughness and estimation of Fermi energy in the graphene nanoribbon (PDF)

AUTHOR INFORMATION

Corresponding Author

Feng Wang – *Department of Physics, University of California at Berkeley, Berkeley, California 94720, United States; Materials Science Division, Lawrence Berkeley National Laboratory, Berkeley, California 94720, United States; Kavli Energy NanoSciences, University of California Berkeley, Berkeley, California 94720, United States*;
Email: fengwang76@berkeley.edu

Authors

Wenyu Zhao – *Department of Physics, University of California at Berkeley, Berkeley, California 94720, United States*; orcid.org/0000-0001-5740-5613

Hongyuan Li – *Department of Physics and Graduate Group in Applied Science and Technology, University of California at Berkeley, Berkeley, California 94720, United States; Materials Science Division, Lawrence Berkeley National Laboratory, Berkeley, California 94720, United States*; orcid.org/0000-0001-9119-5592

Xiao Xiao – *Department of Physics, University of California at Berkeley, Berkeley, California 94720, United States; Department of Physics, Chinese University of Hong Kong, Hong Kong 999077, China*

Yue Jiang – *Department of Physics, University of California at Berkeley, Berkeley, California 94720, United States; Department of Physics, Chinese University of Hong Kong, Hong Kong 999077, China*

Kenji Watanabe – *Research Center for Functional Materials, National Institute for Materials Science, Tsukuba 305-0044, Japan*; orcid.org/0000-0003-3701-8119

Takashi Taniguchi – *International Center for Materials Nanoarchitectonics, National Institute for Materials Science, Tsukuba 305-0044, Japan*; orcid.org/0000-0002-1467-3105

Alex Zettl – *Department of Physics, University of California at Berkeley, Berkeley, California 94720, United States; Materials Science Division, Lawrence Berkeley National Laboratory, Berkeley, California 94720, United States; Kavli*

Energy NanoSciences, University of California Berkeley, Berkeley, California 94720, United States

Complete contact information is available at:
https://pubs.acs.org/10.1021/acs.nanolett.1c00276

Author Contributions

¶(W.Z. and H.L.) These authors contributed equally to this work

Author Contributions

F.W. supervised the project; W.Z. performed the cryogenic near-field measurement; H.L. prepared the samples and devices; and W.Z. performed the numerical simulations. F.W., W.Z., and H.L. analyzed the data. All authors discussed the results and contributed to writing the manuscript.

Notes

The authors declare no competing financial interest.

■ ACKNOWLEDGMENTS

This work was mainly supported by the U.S. Department of Energy, Office of Science, Basic Energy Sciences, Materials Sciences and Engineering Division under the Contract No. DE-AC02-05-CH11231 (sp2-Bonded Materials Program KC2207). The FET device fabrication was supported by the Office of Naval research (MURI Award N00014-16-1-2921). K.W. and T.T. acknowledge support from the Elemental Strategy Initiative conducted by the MEXT, Japan, Grant Number JPMXP0112101001, JSPS KAKENHI Grant Number JP20H00354, and the CREST(JPMJCR15F3), JST.

■ REFERENCES

(1) Christensen, T. Fundamentals of Plasmonics. *From Classical to Quantum Plasmonics in Three and Two Dimensions*; Springer: 2017; pp 13−35.

(2) Novotny, L.; Hecht, B. *Principles of nano-optics*; Cambridge University Press: New York, 2012.

(3) Basov, D. N.; Fogler, M. M.; Garcia de Abajo, F. J. Polaritons in van der Waals materials. *Science* **2016**, *354* (6309), aag1992.

(4) Dai, S.; Fei, Z.; Ma, Q.; Rodin, A.; Wagner, M.; McLeod, A.; Liu, M.; Gannett, W.; Regan, W.; Watanabe, K.; et al. Tunable phonon polaritons in atomically thin van der Waals crystals of boron nitride. *Science* **2014**, *343* (6175), 1125−1129.

(5) Vakil, A.; Engheta, N. Transformation optics using graphene. *Science* **2011**, *332* (6035), 1291−1294.

(6) Bozhevolnyi, S. I.; Martin-Moreno, L.; Garcia-Vidal, F. *Quantum plasmonics*; Springer: Switzerland, 2017.

(7) Yu, N.; Capasso, F. Flat optics with designer metasurfaces. *Nat. Mater.* **2014**, *13* (2), 139−150.

(8) Fu, Y.; Hu, X.; Lu, C.; Yue, S.; Yang, H.; Gong, Q. All-optical logic gates based on nanoscale plasmonic slot waveguides. *Nano Lett.* **2012**, *12* (11), 5784−5790.

(9) Nezhad, M. P.; Tetz, K.; Fainman, Y. Gain assisted propagation of surface plasmon polaritons on planar metallic waveguides. *Opt. Express* **2004**, *12* (17), 4072−4079.

(10) Oulton, R. F.; Sorger, V. J.; Genov, D.; Pile, D.; Zhang, X. A hybrid plasmonic waveguide for subwavelength confinement and long-range propagation. *Nat. Photonics* **2008**, *2* (8), 496−500.

(11) Hu, F.; Luan, Y.; Fei, Z.; Palubski, I.; Goldflam, M.; Dai, S.; Wu, J.-S.; Post, K.; Janssen, G.; Fogler, M.; et al. Imaging the localized plasmon resonance modes in graphene nanoribbons. *Nano Lett.* **2017**, *17* (9), 5423−5428.

(12) Christensen, J.; Manjavacas, A.; Thongrattanasiri, S.; Koppens, F. H.; García de Abajo, F. J. Graphene plasmon waveguiding and hybridization in individual and paired nanoribbons. *ACS Nano* **2012**, *6* (1), 431−440.

(13) Nikitin, A.; Alonso-González, P.; Vélez, S.; Mastel, S.; Centeno, A.; Pesquera, A.; Zurutuza, A.; Casanova, F.; Hueso, L.; Koppens, F.; et al. Real-space mapping of tailored sheet and edge plasmons in graphene nanoresonators. *Nat. Photonics* **2016**, *10* (4), 239−243.

(14) Nikitin, A. Y.; Guinea, F.; García-Vidal, F.; Martín-Moreno, L. Edge and waveguide terahertz surface plasmon modes in graphene microribbons. *Phys. Rev. B: Condens. Matter Mater. Phys.* **2011**, *84* (16), 161407.

(15) Ju, L.; Geng, B.; Horng, J.; Girit, C.; Martin, M.; Hao, Z.; Bechtel, H. A.; Liang, X.; Zettl, A.; Shen, Y. R.; et al. Graphene plasmonics for tunable terahertz metamaterials. *Nat. Nanotechnol.* **2011**, *6* (10), 630−634.

(16) Fei, Z.; Goldflam, M.; Wu, J.-S.; Dai, S.; Wagner, M.; McLeod, A.; Liu, M.; Post, K.; Zhu, S.; Janssen, G.; et al. Edge and surface plasmons in graphene nanoribbons. *Nano Lett.* **2015**, *15* (12), 8271−8276.

(17) Grigorenko, A.; Polini, M.; Novoselov, K. Graphene plasmonics. *Nat. Photonics* **2012**, *6* (11), 749.

(18) Jablan, M.; Soljačić, M.; Buljan, H. Plasmons in graphene: fundamental properties and potential applications. *Proc. IEEE* **2013**, *101* (7), 1689−1704.

(19) Koppens, F. H.; Chang, D. E.; Garcia de Abajo, F. J. Graphene plasmonics: a platform for strong light−matter interactions. *Nano Lett.* **2011**, *11* (8), 3370−3377.

(20) Maier, S. A. *Plasmonics: fundamentals and applications*; Springer Science & Business Media: New York, 2007.

(21) Fei, Z.; Rodin, A.; Andreev, G. O.; Bao, W.; McLeod, A.; Wagner, M.; Zhang, L.; Zhao, Z.; Thiemens, M.; Dominguez, G.; et al. Gate-tuning of graphene plasmons revealed by infrared nano-imaging. *Nature* **2012**, *487* (7405), 82−85.

(22) Ni, G.; McLeod, A.; Sun, Z.; Wang, L.; Xiong, L.; Post, K.; Sunku, S.; Jiang, B.-Y.; Hone, J.; Dean, C. R.; et al. Fundamental limits to graphene plasmonics. *Nature* **2018**, *557* (7706), 530−533.

(23) Woessner, A.; Lundeberg, M. B.; Gao, Y.; Principi, A.; Alonso-González, P.; Carrega, M.; Watanabe, K.; Taniguchi, T.; Vignale, G.; Polini, M.; et al. Highly confined low-loss plasmons in graphene−boron nitride heterostructures. *Nat. Mater.* **2015**, *14* (4), 421−425.

(24) Chen, J.; Badioli, M.; Alonso-González, P.; Thongrattanasiri, S.; Huth, F.; Osmond, J.; Spasenović, M.; Centeno, A.; Pesquera, A.; Godignon, P.; et al. Optical nano-imaging of gate-tunable graphene plasmons. *Nature* **2012**, *487* (7405), 77−81.

(25) Jablan, M.; Buljan, H.; Soljačić, M. Plasmonics in graphene at infrared frequencies. *Phys. Rev. B: Condens. Matter Mater. Phys.* **2009**, *80* (24), 245435.

(26) Silveiro, I.; Ortega, J. M. P.; De Abajo, F. J. G. Quantum nonlocal effects in individual and interacting graphene nanoribbons. *Light: Science & Applications* **2015**, *4* (1), No. e241.

(27) Jiang, X.; Cai, W.; Luo, W.; Xiang, Y.; Zhang, N.; Ren, M.; Zhang, X.; Xu, J. Near-field imaging of graphene triangles patterned by helium ion lithography. *Nanotechnology* **2018**, *29* (38), 385205.

(28) Li, H.; Ying, Z.; Lyu, B.; Deng, A.; Wang, L.; Taniguchi, T.; Watanabe, K.; Shi, Z. Electrode-free anodic oxidation nanolithography of low-dimensional materials. *Nano Lett.* **2018**, *18* (12), 8011−8015.

(29) Li, H.; Li, S.; Naik, M. H.; Xie, J.; Li, X.; Wang, J.; Regan, E.; Wang, D.; Zhao, W.; Zhao, S.; et al. Imaging moiré flat bands in three-dimensional reconstructed WSe2/WS2 superlattices. *Nat. Mater.* **2021**, 1−6.

(30) Ocelic, N.; Huber, A.; Hillenbrand, R. Pseudoheterodyne detection for background-free near-field spectroscopy. *Appl. Phys. Lett.* **2006**, *89* (10), 101124.

https://doi.org/10.1021/acs.nanolett.1c00276
Nano Lett. 2021, 21, 3106−3111